

An Audio Jack-Based Electrochemical Impedance Spectroscopy Sensor for Point-of-Care Diagnostics

Haowei Jiang, *Student Member, IEEE*, Alexander Sun, *Student Member, IEEE*,
Alagarswamy G. Venkatesh, and Drew A. Hall, *Member, IEEE*

Abstract—Portable and easy-to-use point-of-care (POC) diagnostic devices hold high promise for dramatically improving public health and wellness. In this paper, we present a mobile health immunoassay platform based on audio jack-embedded devices, such as smartphones and laptops, that uses electrochemical impedance spectroscopy to detect binding of target biomolecules. This platform is intended to be used as a plug-and-play peripheral that reuses existing hardware in the mobile device, and does not require an external battery, thereby improving upon its convenience and portability. Experimental data using a passive circuit network to mimic an electrochemical cell demonstrate that the device performs comparable to laboratory grade instrumentation with 0.3% and 0.5° magnitude and phase error, respectively, over a 17 Hz–17 kHz frequency range. The measured power consumption is 2.5 mW with a dynamic range of 60 dB. This platform was verified by monitoring the real-time formation of a NeutrAvidin self-assembled monolayer on a gold electrode demonstrating the potential for POC diagnostics.

Index Terms—Electrochemical impedance spectroscopy, mHealth, audio jack, point-of-care testing, electrochemical sensors.

I. INTRODUCTION

DECENTRALIZATION of diagnostic testing from large and expensive clinical laboratories directly to the patients' bedside or home has been a focus of researchers for many years and is a key component of the current precision medicine initiative [1], [2]. This portable diagnostic infrastructure would not only allow physicians to make fast and accurate diagnoses, but also decrease medical costs and reduce turnaround time for the patient. Such technology would even enable the patient to routinely and remotely monitor his or her disease progression and treatment effectiveness remotely. Hence, there is a strong demand for point-of-care (POC) biomolecular sensor platforms that are affordable, portable, and user-friendly. These POC tests need to be both

Manuscript received September 23, 2016; revised November 28, 2016; accepted November 29, 2016. Date of publication December 1, 2016; date of current version January 6, 2017. This work was supported in part by the U.S. Agency for International Development under Grant AID-OAA-A-13-00002 and in part by the National Institutes of Health under Grant UL1TR000100. The associate editor coordinating the review of this paper and approving it for publication was Dr. Chang-Soo Kim.

H. Jiang, A. Sun, and D. A. Hall are with the Department of Electrical and Computer Engineering, University of California at San Diego, La Jolla, CA 92093 USA (e-mail: drewhall@ucsd.edu).

A. G. Venkatesh was with the Department of Electrical and Computer Engineering, University of California at San Diego, La Jolla, CA 92093 USA. He is now with Roswell Biotechnology Inc., San Diego, CA 92121 USA.

Digital Object Identifier 10.1109/JSEN.2016.2634530

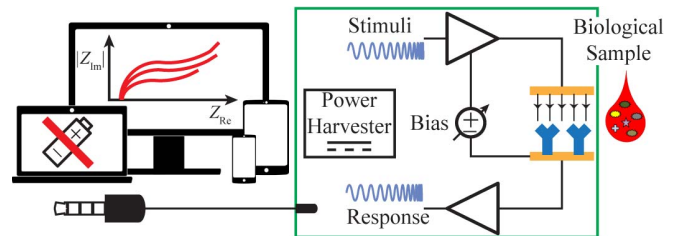


Fig. 1. Overview of the proposed audio jack-based EIS sensor.

rapid and sensitive while utilizing well established immunoassay chemistries [3]. Although, to date, the most successful biosensor has been the glucometer, recent advances in mobile technologies have made more general purpose biomolecular sensors both feasible and practical [4]–[9].

Currently, more than one-quarter of the global population use smartphones with a projected increase to over one-third of consumers worldwide in 2018. Among new smartphone owners, 80% percent will be from developing countries and rural areas where medical facilities are limited and/or inaccessible [10]. Fortunately, smartphones offer an opportunity to develop affordable and reliable POC diagnostic tools to supplement the current infrastructure [11]. Its powerful integrated functionality, e.g., CPUs with advanced computation capability, RAMs with large storage, wireless radios that support multiple standards, large user-friendly touchscreens, and high-resolution ADC/DACs embedded in the audio channels, make the smartphone an ideal platform for interfacing sensors. Aside from smartphones, personal computers (PCs), laptops and tablets, the usage of which is also booming in developing countries and rural areas, are similarly excellent candidates for building POC devices.

On the sensor side, electrochemical techniques, in particular electrochemical impedance spectroscopy (EIS), have received considerable attention for POC biosensors [12]–[17]. EIS measures the impedance between two electrodes of an electrochemical cell by applying a small-signal voltage tone at different frequencies and measuring the resulting small-signal current. Since the impedance changes as a result of biomolecules (analytes) binding to ligands immobilized on the surface of the electrode, EIS is a label-free, real-time, and wash-free testing technique [18]. Such features are quintessential characteristics in POC applications where it necessary to reduce

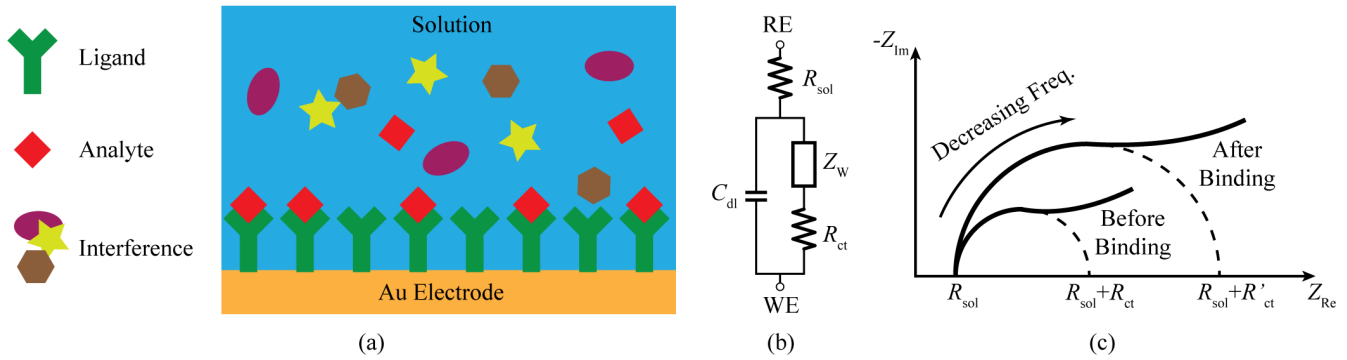


Fig. 2. (a) Illustration of surface binding process. (b) Typical Randles circuit model of F-EIS. (c) Nyquist plot of a typical Randles circuit.

the number of assay steps, time, and reagents. Specifically, when compared to other surface-based affinity assays, e.g. the classical enzyme linked immunosorbent assay (ELISA), which require washing steps to remove unbound analytes, ligands, and labels, EIS holds more promise for portable immunoassay platforms, as no secondary labeling or washing is required [7], [18].

Here we present the development of a mobile health (mHealth) EIS immunoassay platform that interfaces with mobile devices via the audio jack (Fig. 1). The 3.5-mm 4-ring audio jack is standard across nearly all mobile devices including smartphones, tablets, and laptops, whereas USB or proprietary ports are not. This choice of port guarantees uniformity in design and compatibility with virtually all devices in any environment. Compared to other smartphone or audio jack-based electrochemistry biosensors, this work utilizes the mobile device for functions that typically require extraneous parts, such as batteries, microcontrollers, and communication modules (e.g., Wi-Fi or Bluetooth) [12]–[15]. Figure 1 illustrates the key components in the system. The left audio playback channel is used to power the device and set the DC bias potential between the two electrodes, whereas the right channel generates the AC stimuli for the sensor and controls the switching between the different sensors. The microphone is used to capture the response from the sensors. The host device's CPU then processes the data locally. Operating the device is as simple as plugging the device into a headphone jack, running the application, and adding the sample. Combined with gold electrodes functionalized with a ligand for specificity, this device can detect the presence of a biomarker from an unknown solution while simultaneously measuring a negative control and two calibration channels.

The size of the device is 3.2×2.6 in. (approximately the size of a credit card), so that it can be held and transported conveniently. A graphical user interface was developed to control the EIS measurement and visualize the measurement results. By designing the device to push all of data conversion and signal processing to the host device, additional system-on-chip (SoC) components, e.g. microcontrollers, ADCs/DACs, and communication modules are no longer required reducing the overall cost of the device [12]–[15].

The rest of the paper is organized as follows. Section II describes the design of the EIS sensing platform along with

a brief review of EIS. An impedance extraction algorithm is proposed in Section III that improves the accuracy of the impedance measurements. Sections IV and V present electrical and biological measurement results, respectively. A comparison to existing work is shown in Section VI and conclusions are drawn in Section VII.

II. SYSTEM OVERVIEW

A. Operating Principle

In EIS, the sensing electrode is functionalized with a ligand complimentary to the target analyte and subsequently blocked to minimize non-specific binding as shown in Fig. 2(a). The ligand is what provides specificity against off-target binding. As the target analytes bind to the surface immobilized ligands, the local (Helmholtz region) charge is disturbed resulting in a change in impedance. This electrochemical cell can be modeled by the Randles circuit shown in Fig. 2(b) that consists of: the solution resistance R_{sol} , the Warburg impedance Z_w , the double-layer capacitance C_{dl} , and the charge transfer resistance R_{ct} . This work uses Faradaic EIS (f-EIS), wherein reversible redox molecules are present in the solution to facilitate charge transfer between the electrodes thus amplifying the change in R_{ct} when the electrode surface is perturbed. In most cases, molecules that bind to the surface of the electrode inhibit the redox reaction from occurring and thus increase R_{ct} [19]. Hence, in f-EIS, R_{ct} is used to track the ligand-analyte binding.

A two electrode architecture is adopted where the test stimuli is applied to the reference electrode (RE) and the current is measured at the ligand functionalized working electrode (WE). A representative Nyquist plot of the impedance for a Faradaic Randles circuit is shown in Fig. 2(c). At high frequencies, the Nyquist curve is approximately a semicircle so, by fitting the high frequency part of the curve, the value of R_{ct} can be extracted from the semicircle diameter. Note that the charge transfer resistance R_{ct} can also be affected by temperature, pH, DC bias, and non-specific binding. To eliminate these sources of variation, a negative control sensor (blocked without functionalization towards a specific analyte) is used, where no binding should occur.

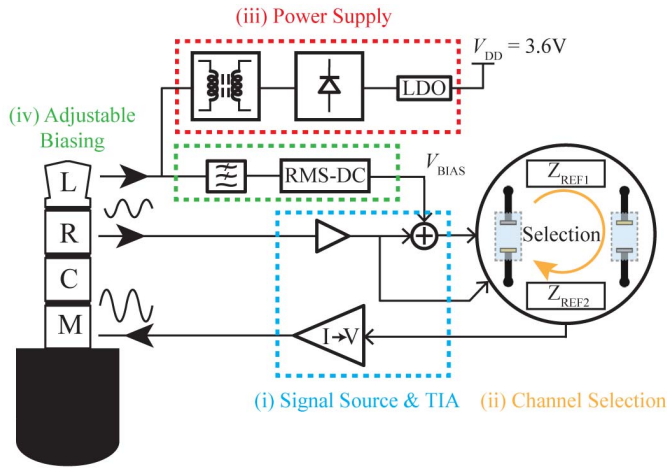


Fig. 3. Architecture of the audio jack-based EIS sensor.

B. Architecture

A block diagram of the audio jack-based EIS sensing system is shown in Fig. 3. Conceptually, the system is designed to apply a small-signal AC excitation (5 mV_{pk}) on top of a DC bias to one of the sensors and send the response back to the host device. When implementing this device using only the audio jack, there are certain challenges that need to be addressed. First, there are only two output channels (left and right), but the host needs to supply four signals – power, an AC stimulus, a DC bias voltage, and a control signal to select the sensor to be measured. Therefore, the audio outputs must be reused for multiple functions. Second, the audio channels are AC coupled, meaning that DC voltages, such as for the power and DC bias, cannot be directly transmitted to the peripheral device. Third, the frequency range is limited to the audio band, 15 Hz - 20 kHz. Fourth, the frequency response of the microphone input is not known nor consistent across different phone makes and models. Lastly, due to the host firmware, the ADC and DAC cannot be synchronized. Together, these constraints impose challenges that must be addressed at the circuit and system level. At the system level, the left audio channel is frequency duplexed by powering up the device with a high frequency tone and setting the bias potential with a low frequency tone; the right audio channel is time multiplexed to switch and stimulate electrochemical sensor channels. The following sections describe how each of the sub-circuits are implemented.

C. Signal Source and TIA

The stimulus signal is generated by the DAC on the host device and sent through the right audio channel where it is superimposed on the adjustable DC bias voltage and applied to the RE of each sensor, as shown in Fig. 4. There are four sensors – two reference impedances for calibration (discussed below) and two devices under test (DUT). The superposition of stimulus and bias is realized with a summing amplifier. The WEs of the sensors connect to the virtual ground node of the transimpedance amplifier (TIA) via a 4:1 multiplexer. Stability issues were carefully considered in designing the summing

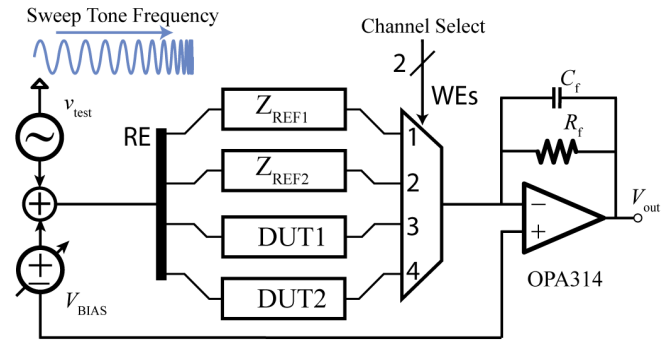


Fig. 4. Simplified schematic of the signal path, including the signal source, four test channels (two sensors and two reference impedances), and the TIA.

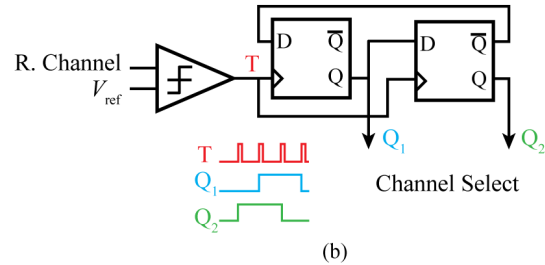
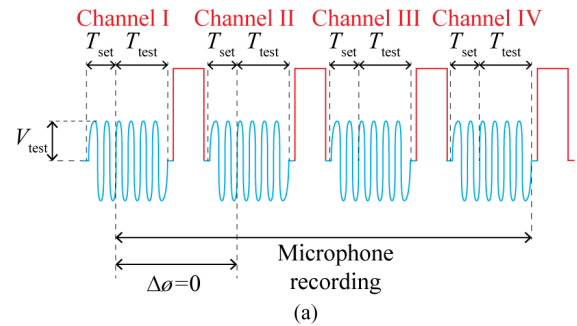


Fig. 5. (a) Timing diagram of the stimuli and switch markers. (b) Circuit implementation of switch control and timing diagram of the control signals.

amplifier since the large parasitic capacitance of the mux and sensors can lead to instability. For this reason, the mux is only placed at the WE rather than on both sides of the sensors. Both the signal source and TIA must have a high gain bandwidth product to ensure good linearity across the entire frequency range. An op-amp with resistive feedback was used for the TIA with a film capacitor, which has a low voltage coefficient improving its linearity compared to other types of capacitors.

Since electrochemical cells are mostly capacitive, the impedance reduces as the frequency is increased, and for a fixed amplitude stimulus, the resulting current increases. If the TIA gain was constant versus frequency, the TIA output could saturate the microphone ADC at high frequencies, while the signal-to-noise ratio (SNR) might be insufficient at low frequencies. To extend the dynamic range (DR), the TIA corner frequency was set to 0.7 kHz, which is lower than the maximum frequency so that the TIA gain (3.3 kΩ) rolls off at high frequencies to prevent saturation.

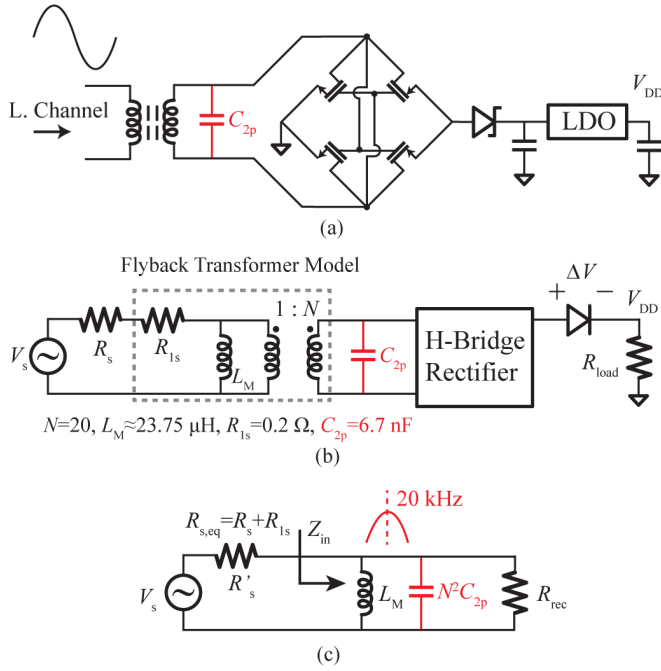


Fig. 6. (a) Power harvester topology from [20], and the added parallel capacitor in red. (b) Equivalent circuit model. (c) Simplified circuit model for analysis.

D. Sensor Selection

The right audio channel was also used to select which sensor to measure. As shown in Fig. 5(a), after applying the sinusoidal stimulus for a settling period T_{set} and measurement period T_{test} , a high amplitude marker is sent to select the next sensor. This is done four times to select each of the sensors after which the frequency steps to the next value and the process repeats. The pulse triggers a comparator and a 2-bit counter (two cascaded D flip-flops) to control the multiplexer, as shown in Fig. 5(b). A start-up circuit always selects channel 1 when the device is first powered up. This switching scheme ensures that the stimuli at each frequency interval are in phase with each other. Since it takes $\sim 100 \text{ ms}$ for the TIA to settle after switching, data from T_{set} is discarded.

E. Power Harvester

In most commercial audio chipsets, a power amplifier follows the DAC to drive low impedance ($\sim 3 \Omega$) headphones. We have previously reported a power harvesting circuit capable of extracting 5.7 mW from an iPhone 5s, as shown in Fig. 6(a) [20]. The circuit operates as follows: a 15-20 kHz AC tone from the audio port is stepped up by a flyback transformer, rectified by a MOSFET H-bridge, and then regulated to a 3.6 V V_{DD} by a Schottky diode and an LDO. An augmented design with tunable impedance matching and DC-DC converter has been reported to be capable of extracting 18.7 mW from an iPhone 4 with an efficiency of 79% [4], [21]. However, it requires a microcontroller to tune the input frequency, which may fall into the EIS measurement region. In this design, the left channel also needs to provide the adjustable DC bias which requires 30% of the full scale range

leaving only 70% of the swing for power harvesting. Since the power delivered to the load is proportional to V^2 , this is a substantial deviation from the previous work and requires changes in the design to improve the efficiency.

Figure 6(b) shows the circuit model of the power harvester including a model of the flyback transformer that is modeled as a magnetizing inductor L_M in parallel with an ideal 1:N transformer. The series resistor at the primary side R_{1s} is lumped into the source resistance R_s of audio output as effective source resistance $R_{s,eq}$. All of the circuits following the LDO can be modeled as a load resistor R_{load} :

$$R_{load} = \frac{V_{DD}^2}{P} \quad (1)$$

where P is the power consumption and V_{DD} is the supply voltage. Since both the Schottky diode and the LDO have a constant dropout voltage, they can be modeled as an ideal diode with forward-voltage ΔV , as shown in Fig. 6(b). Assuming the H-bridge rectifier is lossless, the load impedance reflected to the primary side of the transformer (Fig. 6c) can be derived as:

$$R_{rec} = \frac{(V_{DD} + \Delta V) V_{DD}}{N^2 P}. \quad (2)$$

Subsequently, the allowable circuit supply voltage is given by

$$V_{DD} = N \left| \frac{Z_{in}}{Z_{in} + R_{s,eq}} \right| V_s - \Delta V \quad (3)$$

where V_s is the RMS voltage from the audio output. In this design, V_{DD} must be $> 3.6 \text{ V}$ for proper operation. However, the load voltage is limited by the small impedance of the magnetizing inductor, $\sim 3 \Omega$ at 20 kHz. Since this is comparable to R_{rec} , a large portion of current would go through the magnetizing inductor diminishing the available power.

To remedy this, a capacitor C_{2p} is placed in parallel with the secondary side of the transformer, as shown in Fig. 6(a). Similar to reactive power compensation, which is widely used in power systems [22], C_{2p} resonates out the reactive impedance of the transformer making the input impedance purely real. As such, no reactive power is stored in the transformer and maximum power can be delivered to the load. In order to minimize interference, the tone frequency is chosen at 20 kHz, which is above the maximum EIS frequency range.

The transformer ratio N needs to be carefully chosen to maximize the driving ability, which is the maximum power that can be delivered to the load. By setting V_{DD} based on signal swing and minimum supply voltage, the delivered power can be derived from Eq. (2) and (3) as a function of N where

$$P = -\frac{1}{R_{s,eq}} \left(\frac{V_{DD}}{N} - \frac{V_s - \frac{\Delta V}{N}}{2} \right)^2 + \frac{(V_s - \frac{\Delta V}{N})^2}{4R_{s,eq}}. \quad (4)$$

The driving ability is optimized when $(V_s - \Delta V/N)/2$ (around half of the source voltage) is equal to V_{DD}/N , which is the case of matching, i.e. $Z_{in} = R'_s$. Considering the range of R_s and V_s (discussed in section IV), the optimal value of N is 20.

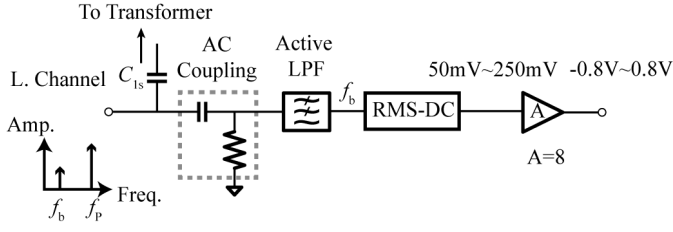


Fig. 7. Simplified schematic of the adjustable DC bias circuit.

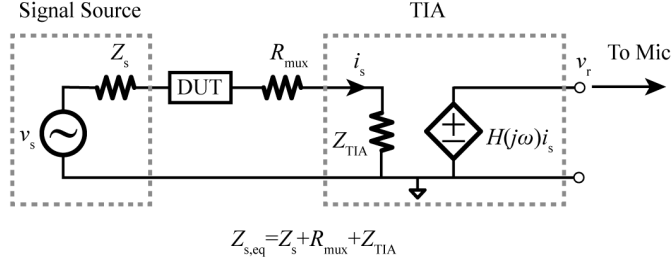


Fig. 8. Measurement circuit model of signal source, DUT, and TIA.

F. Adjustable DC Bias

In f-EIS, the electrode bias voltage needs to be set properly because the redox reaction rate and direction depend on the potential applied between the electrodes. To prevent the reaction from being driven to one side (i.e., all oxidized or all reduced), the WE must be biased at the standard potential for a pair of redox molecules. In addition to the 20 kHz tone f_p used for the power supply, a tone f_b is superimposed on the left audio output for the bias circuit, as shown in Fig. 7. After the AC coupling, the low frequency tone f_b passes through both a low-pass filter (LPF), where f_p is highly attenuated, and an RMS-to-DC converter. Finally, the DC bias signal is amplified and another LPF attenuates the ripple and 2nd order harmonics produced by the RMS-to-DC converter. A 10 μ F capacitor C_{1s} decouples the bias circuit from the power harvesting circuit. The DC bias voltage can be controlled linearly by the amplitude of the bias tone on left channel. To achieve at least 40 dB of attenuation, f_b is set to 100 Hz.

III. IMPEDANCE EXTRACTION ALGORITHM

Both the magnitude and phase information of the sensor need to be extracted. The equivalent circuit model of the system is shown in Fig. 8. Conventionally, the impedance is determined by characterizing the transfer function of $H(j\omega)$ of the signal path. When combined with the stimulus v_s and response v_r , one can calculate the impedance Z_{DUT} as follows (assuming $Z_{DUT} \gg Z_{s,eq}$):

$$Z_{DUT} = -H(j\omega) \frac{v_r}{v_s}. \quad (5)$$

However, the transfer function $H(j\omega)$ strongly depends on the gain accuracy gain of the TIA, as well as the unknown filter(s) inherent within the microphone channel. If this is not accounted for, the frequency range is limited to between 50 Hz and 10 kHz. Moreover, it is not possible to synchronize

TABLE I
SUMMARY OF POWER HARVESTING

Parameter	iPhone 4s/5/5s/6 (iOS phone)	Samsung Note-4 (Android phone)	Dell T3610 (PC)
V_s (V _{RMS})	0.48	0.42	0.70
R_s (Ω)	3.0	1.8	19.9
$R_{s,eq}$ (Ω)	3.2	2	20.1
V_{DD} (V)	3.64	3.64	3.64
Maximum	16.9	11.0	5.8
P_{load} (mW)			

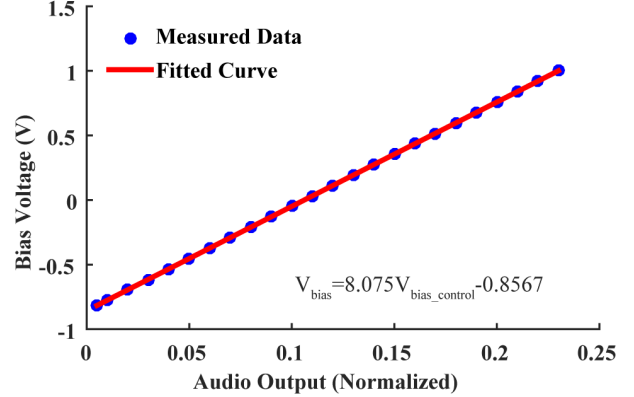


Fig. 9. Measured bias voltage vs. audio output normalized to the full scale range.

the sampling of the ADC and DAC inside of the audio port due to firmware limitations, thus only magnitude information can be acquired using this approach [15].

These issues were addressed by adding two reference channels to compensate for the variability in $H(j\omega)$ and determine the relative phase information. The reference channels are nominally identical to the test channel as they are excited with the same v_s and measured with the same TIA. However, instead of measuring an electrochemical cell, these channels are connected to fixed known impedances $Z_{REF1,2}$ that can be accurately characterized [23]. According to the measurement circuit model in Fig. 8, the impedance of the DUT is then given by:

$$Z_{DUT} = Z_{REF} \frac{v_{rDUT}}{v_{rREF}} + Z_{s,eq} \left(\frac{v_{rDUT}}{v_{rREF}} - 1 \right) \approx Z_{REF} \frac{v_{rDUT}}{v_{rREF}} \quad (6)$$

where $Z_{s,eq}$ is the effective source impedance, which contains the output impedance of the summing amplifier, resistance of the mux, and TIA input impedance. Since Z_s is very small ($<10 \Omega$) compared to the solution resistance between electrodes, the term with Z_s is neglected [23]. However, compared with similar work where power consumption was not a major concern, the source impedance term in a low power design may cause high frequency errors (close to 20 kHz), which cannot be neglected. Thus, two reference channels were used instead of one. The small-signal impedance of the DUT

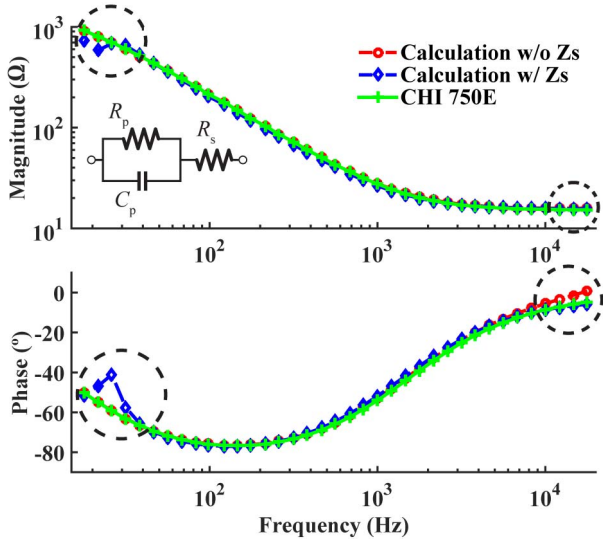


Fig. 10. Comparison of measured impedance spectra of the mock electrochemical cell using different impedance extraction algorithms.

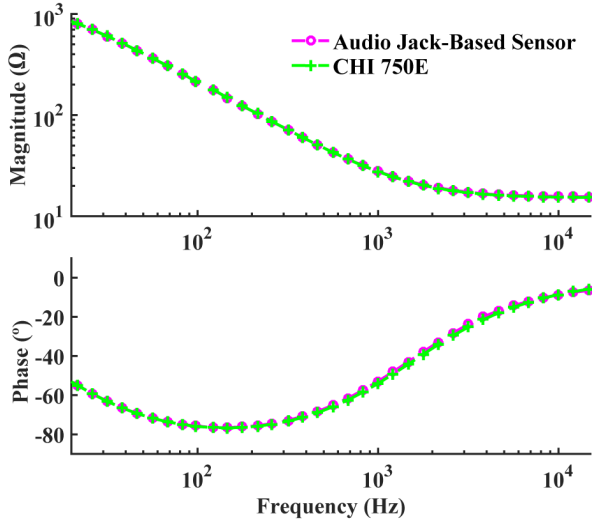


Fig. 11. Measured impedance spectra of the mock electrochemical cell.

is then:

$$Z_{DUT} = \frac{v_{TREF1} v_{TREF2} (Z_{REF2} - Z_{REF1})}{v_{DUT} (v_{TREF1} - v_{TREF2}) - \frac{v_{TREF2} Z_{REF2} - v_{TREF1} Z_{REF1}}{v_{TREF1} - v_{TREF2}}} \quad (7)$$

The phase information is acquired by measuring the response of each of the reference channels and the two sensors. In this way, the relative phase offset between the stimulus and response can be calculated and calibrated.

IV. ELECTRICAL MEASUREMENT RESULTS

Prior to wet experiments, we verified the performance of the audio jack-based EIS sensor using passive elements. The mock electrochemical cell mimics the Randles circuit model of a Faradaic electrode (Fig. 2b) with $C_{dl} = 10\mu\text{F}$, $R_{ct} = 1.5\text{k}\Omega$, and $R_{sol} = 15\Omega$. Measurements were also carried out on a

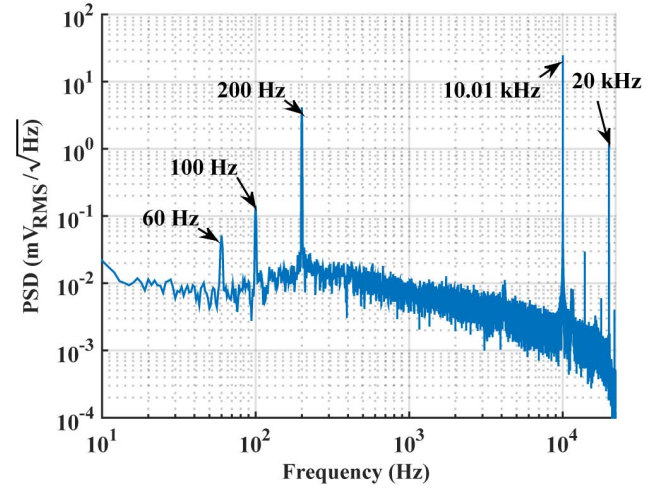


Fig. 12. Measured power spectrum density at the microphone input.

benchtop electrochemical workstation (CH Instruments 750E) for comparison. The mock cell was used for all measurements.

A. Power Consumption

The measured supply voltage was 3.64 V with a quiescent and peak power consumption of 2.3 mW and 2.5 mW, respectively. Measurement results using the sound card of a PC (Dell T3610) showed that 5.1 mW of power was available using 70% of the voltage swing whereas only 1.33 mW was available using the previous topology without the resonant capacitor under the same conditions. The device was also tested with several host-devices (Table I) confirming that, despite the variation in available power and source impedance, the circuit is able to function properly and harvest sufficient power.

B. Bias Calibration

The DC bias voltage needs to cover the -0.8 V to 1.0 V range relative to the WE voltage for most common redox molecules. Fig. 9 shows the measured bias voltage as a function of the amplitude of the tone injected on the left audio channel (0.5% to 25% full scale). The response is very linear with a root-mean-square error of 0.36 mV that comes from the non-linearity of the RMS-DC converter and noise from the LPF.

C. Impedance Measurements With Mock Cell

Fig. 10 shows measured impedance spectra from the mock electrochemical cell using both the audio jack-based EIS platform and the benchtop instrument. Impedance results are shown using two different impedance extraction algorithms: one that ignores Z_s and another that incorporates Z_s . Eq (6) was used to calculate the impedance spectrum which neglects the signal source impedance Z_s . Compared with the CHI, the spectra match well in the low frequency range; however, there is noticeable phase error at higher frequencies. Yet, if Z_s is taken into consideration for the entire frequency range

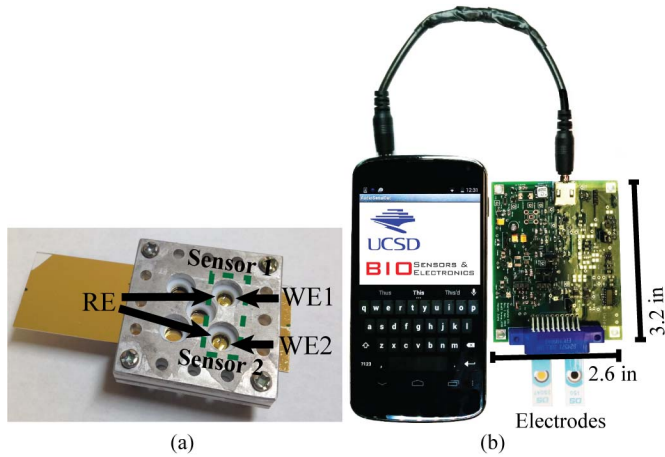


Fig. 13. (a) Photograph of the custom sputtered gold electrodes. (b) Photograph of the PCB prototype EIS system with screen-printed electrodes.

using (7) to calculate the impedance spectrum, both magnitude and phase errors appear at low frequencies. Both equations give comparable results mid-band. As such, we propose to use both equations in their appropriate region, (6) below 5 kHz and (7) above 5 kHz. According to the op-amp and mux datasheets, the source impedance and on-resistance are virtually negligible compared to the DUT impedance at low frequency. When Z_s has less influence than other factors such as noise and non-linearity of the signal path, the circuit model with Z_s in Fig. 4 is no longer a suitable fit to this measured data. As a result, it is more accurate to assume Z_s to be zero in the low frequency region.

The impedance spectrum from the combined circuit model is shown in Fig. 11. Both the magnitude and phase closely match with measurement results from the electrochemical workstation. The maximum magnitude error is 1.1% with a standard deviation of 0.3% and the phase error is less than 1.3° with a standard deviation of 0.5° .

D. Limit of Detection

The spectrum of the acquired signal from the microphone is presented in Fig. 12. The input test signal is at 10.01 kHz, the largest tone shown in the plot. Other significant tones include: 60 Hz power-line interference, 100 Hz and 200 Hz ripple from the RMS-DC converter, and 20 kHz interference from the power harvester. Since the effective bandwidth of the FFT (BW_{FFT}) is $2/3$ Hz, the SNR is not diminished by the interference. The SNR at each frequency is determined by the following equation:

$$\text{SNR}(f) = 20 \log_{10} \frac{\frac{V_s}{\sqrt{2}Z_{DUT}(f)}}{i_n(f)\sqrt{BW_{FFT}}} \quad (8)$$

where V_s is the amplitude of the input stimulus and $\overline{i_n(f)}$ is the input-referred current noise. With an $\overline{i_n(f)}$ of 2.45 nA_{RMS} for a V_s of 5 mV_{pk}, the DUT impedance should be less than 14.4 k Ω to maintain an SNR greater than 40 dB, which ensures <1% error. The system has a DR of 60 dB or 10 Ω – 10 k Ω .

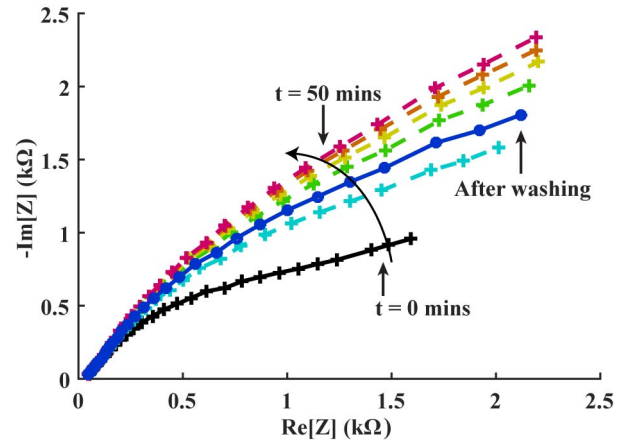


Fig. 14. Nyquist plot showing NeutrAvidin binding on electrode surface over time.

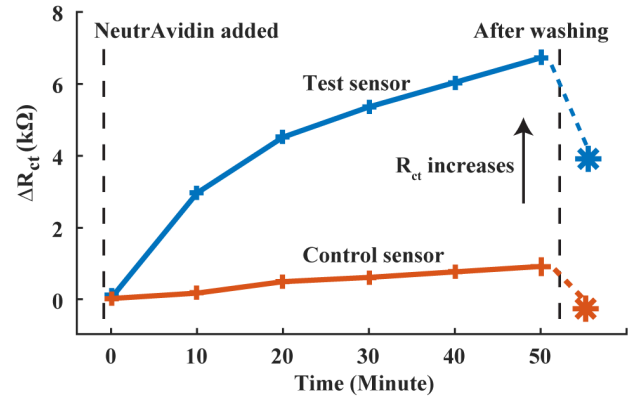


Fig. 15. Change in charge transfer resistance R_{ct} of test and control sensors over time.

V. ELECTROCHEMICAL MEASUREMENTS

Immobilization of detection molecules, such as self-assembled monolayers (SAMs), on gold electrodes has been extensively used for biological detection [24]. The formation of the monolayers modulates the interfacial electron-transfer kinetics that lead to an increase in R_{ct} . The audio jack-based EIS sensor was used to measure this R_{ct} change and detect the real-time binding of NeutrAvidin with a biotinylated SAM.

A. Experiment Setup

A custom sensor with sputtered gold electrodes was fabricated. Glass slides sputtered with 10 nm Cr and 200 nm gold were used for the working and reference electrodes due to their superior impedance spectra in the appropriate frequency range compared to that of screen printed electrodes [25]. The sputtered glass slide with continuous gold film was segmented with a diamond-tipped pen to pattern two WEs and one common RE as shown in Fig. 13. The slides were mounted in a custom fixture to create a fluidic chamber on top of the electrode. Prior to setting up the electrodes, the holder components and gold surface were thoroughly cleaned to remove organics. The self-assembled monolayer of biotin was formed on the gold surface by treating it

TABLE II
PERFORMANCE COMPARISON

SPEC	[10]	[11]	[12]	This Work
Frequency Range	10 kHz – 1 MHz	1 Hz – 10 kHz	50 Hz – 10 kHz	17 Hz – 17 kHz
Dynamic Range	60 dB	N/A	39 dB	60 dB
Accuracy (Mag./Phase)	1% - 2% / N/A	2% / 1°	1% / N/A	0.3% / 0.5°
Analyte	2,4,6-trinitrotoluene	E. Coil	N/A	NeutrAvidin
Connectivity	Bluetooth	USB	Audio jack	Audio jack
Requires Battery?	Yes	No	Yes	No
Bias Voltage	Fixed	Fixed	Fixed	Adjustable

with 2.5 μL biotin-SAM formation reagent (Product #31000, Thermo Fisher Scientific) in 25 μL 1 \times phosphate buffered saline (PBS) at room temperature for 3 hours and washed with 1 \times PBS.

We used 1 mM effective concentration of Ferri/Ferro solution [equal parts potassium ferricyanide ($\text{K}_3[\text{Fe}(\text{CN})_6]$) and potassium ferrocyanide ($\text{K}_4[\text{Fe}(\text{CN})_6]$) in 1 \times PBS] as the redox molecules to magnify the change in charge transfer resistance, R_{ct} . Prior to running the EIS measurement, the redox potential for the Ferri/Ferro solution was measured using cyclic voltammetry (CV) with a scan range between -0.3 V and $+0.3$ V at a rate of 25 mV/s using the CHI 750. The voltages corresponding to the anodic and cathodic current peaks of the resulting CV curve were averaged to find the redox potential of Ferri/Ferro, which was 0 V, as expected. The negative control consists of only 1 mM Ferri/Ferro in PBS, whereas the test contains 0.5 μM NeutrAvidin along with 1 mM Ferri/Ferro.

B. Experimental Results

After powering up the EIS sensor with the audio jack, the bias potential between WE and RE was set to be 0 V for both the test channel and negative control channel. After the test solution was dropped on to sensors, an EIS measurement was taken every 10 minutes. The trend of R_{ct} , which can be determined visually by finding the semicircle radius at the high and mid-frequency region of the Nyquist plot, increased over the span of an hour and reached saturation as shown in Fig. 14. Afterwards, the wells were washed with PBS and then tested again. The R_{ct} values were calculated by fitting the raw EIS data to the Randles circuit model in Fig. 2(b).

The R_{ct} curve of the test sensor exhibits traditional binding characteristics with the resistance increasing exponentially over time ($\Delta R_{\text{ct}} = 6.7$ k Ω), as shown in Fig. 15. The curve of the reference sensor gradually increases over time as well; however, the increase is much less significant (892 Ω) and does not show an exponential trend. This difference suggests that specific binding occurred on the functionalized test sensor, while non-specific binding occurred on the control, possibly due to insufficient blocking of the surface. This is confirmed after washing where the control sensor drops to the original value whereas the test sensor is only partially reduced.

VI. COMPARISON

Table II presents recently published state-of-art portable EIS sensors. Compared with other sensors, this work does not

require an external power source (i.e., a battery) and has the lowest power consumption. It also shows the greatest accuracy in both magnitude and phase over the three-decade frequency range. Owing to the non-flat gain of the TIA and algorithm cancelling source impedance, the DR is expanded to 60 dB. Moreover, it has the ability to adjust the bias potential while others cannot, which is essential for f-EIS measurements.

VII. CONCLUSION

In this paper, we describe the development of a low cost self-powered audio jack-based EIS sensor for point-of-care diagnostics. Compared with other portable impedance sensors, this device uses the audio jack of its host to generate the AC stimuli and receive the response from the sensors. Furthermore, the audio port also supplies power and the necessary test controls to the sensor readout, such that no external battery, microcontroller, or communication modules are required. Two approaches including multiple-modulated AC tones and time-multiplexed sequences are implemented in order to fully utilize limited audio channels, and a revised power harvesting circuit was designed to harvest maximum power from the audio port despite the port also being used to generate a bias voltage.

The audio jack-based EIS sensor demonstrated accurate impedance measurements with the proposed impedance extraction algorithm achieving a magnitude and phase accuracy of a 0.3% and 0.5°, respectively, compared to a laboratory scale electrochemical workstation. For the electrochemical measurement with biotin-SAMs, 0.5 μM of NeutrAvidin was detected successfully. By fitting the measurement results to Randles circuit model, the exponential response curve was monitored. In summary, the audio jack-based EIS sensor provides a promising immunoassay platform for probe-target monitoring for point-of-care testing.

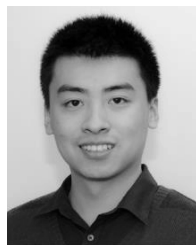
ACKNOWLEDGMENT

The authors would like to thank Brandon Hong for fabricating the sputtered gold electrodes.

REFERENCES

- [1] J. Wang, "Electrochemical biosensors: Towards point-of-care cancer diagnostics," *Biosens. Bioelectron.*, vol. 21, no. 10, pp. 1887–1892, Apr. 2006.
- [2] E. A. Ashley, "The precision medicine initiative: A new national effort," *JAMA*, vol. 313, no. 21, pp. 2119–2120, Jun. 2015.
- [3] P. von Lode, "Point-of-care immunotesting: Approaching the analytical performance of central laboratory methods," *Clin. Biochem.*, vol. 38, no. 7, pp. 591–606, Jul. 2005.

- [4] A. C. Sun, C. Yao, A. G. Venkatesh, and D. A. Hall, "An efficient power harvesting mobile phone-based electrochemical biosensor for point-of-care health monitoring," *Sens. Actuat. B Chem.*, vol. 235, pp. 126–135, Nov. 2016.
- [5] A. Hassibi and T. H. Lee, "A programmable 0.18- μm CMOS electrochemical sensor microarray for biomolecular detection," *IEEE Sensors J.*, vol. 6, no. 6, pp. 1380–1388, Dec. 2006.
- [6] P. B. Lillehoj, M.-C. Huang, N. Truong, and C.-M. Ho, "Rapid electrochemical detection on a mobile phone," *Lab. Chip*, vol. 13, no. 15, pp. 2950–2955, Jul. 2013.
- [7] X. Liu, L. Li, and A. J. Mason, "High-throughput impedance spectroscopy biosensor array chip," *Philos. Trans. R. Soc. London Math. Phys. Eng. Sci.*, vol. 372, no. 2012, p. 20130107, Mar. 2014.
- [8] A. Sun, T. Wambach, A. G. Venkatesh, and D. A. Hall, "A multi-technique reconfigurable electrochemical biosensor for integration into mobile technologies," in *Proc. IEEE Biomed. Circuits Syst. Conf. (BioCAS)*, Oct. 2015, pp. 1–4.
- [9] W. Gao *et al.*, "Fully integrated wearable sensor arrays for multiplexed *in situ* perspiration analysis," *Nature*, vol. 529, no. 7587, pp. 509–514, Jan. 2016.
- [10] A. Boxall. *The Number of Smartphone Users in the World is Expected to Reach a Giant 6.1 Billion by 2020*, *Digital Trends*. Accessed on Sep. 10, 2015. [Online]. Available: <http://www.digitaltrends.com/mobile/smartphone-users-number-6-1-billion-by-2020/>
- [11] A. Ozcan, "Mobile phones democratize and cultivate next-generation imaging, diagnostics and measurement tools," *Lab. Chip*, vol. 14, no. 17, pp. 3187–3194, Sep. 2014.
- [12] J. Jiang *et al.*, "Smartphone based portable bacteria pre-concentrating microfluidic sensor and impedance sensing system," *Sens. Actuators B, Chem.*, vol. 193, pp. 653–659, Mar. 2014.
- [13] D. Zhang *et al.*, "Smartphone-based portable biosensing system using impedance measurement with printed electrodes for 2,4,6-trinitrotoluene (TNT) detection," *Biosens. Bioelectron.*, vol. 70, pp. 81–88, Aug. 2015.
- [14] X. Huang, H. Chen, H. Deng, L. Wang, S. Liao, and A. Tang, "A fast and simple electrochemical impedance spectroscopy measurement technique and its application in portable, low-cost instrument for impedimetric biosensing," *J. Electroanal. Chem.*, vol. 657, nos. 1–2, pp. 158–163, Jul. 2011.
- [15] J. Broeders *et al.*, "Mobile application for impedance-based biomimetic sensor readout," *IEEE Sensors J.*, vol. 13, no. 7, pp. 2659–2665, Jul. 2013.
- [16] J. Punter-Villagrasa *et al.*, "Towards a portable point-of-use blood analysis with EIS technique device," in *Proc. 11th Int. Multi-Conf. Syst., Signals Devices (SSD)*, Feb. 2014, pp. 1–6.
- [17] T. Le, G. Salles-Loustau, L. Najafzadeh, M. Javanmard, and S. Zonouz, "Secure point-of-care medical diagnostics via trusted sensing and cyto-coded passwords," in *Proc. 46th Annu. IEEE/IFIP Int. Conf. Dependable Syst. Netw. (DSN)*, Jun. 2016, pp. 583–594.
- [18] J. S. Daniels and N. Pourmand, "Label-free impedance biosensors: Opportunities and challenges," *Electroanalysis*, vol. 19, no. 12, pp. 1239–1257, Jun. 2007.
- [19] T. Komura, T. Yamaguchi, H. Shimatani, and R. Okushio, "Interfacial charge-transfer resistance at ionizable thiol monolayer-modified gold electrodes as studied by impedance spectroscopy," *Electrochimica Acta*, vol. 49, no. 4, pp. 597–606, Feb. 2004.
- [20] A. Sun, T. Wambach, A. G. Venkatesh, and D. A. Hall, "A low-cost smartphone-based electrochemical biosensor for point-of-care diagnostics," in *Proc. IEEE Biomed. Circuits Syst. Conf. (BioCAS)*, Oct. 2014, pp. 312–315.
- [21] C. Yao, A. Sun, and D. A. Hall, "Efficient power harvesting from the mobile phone audio jack for mHealth peripherals," in *Proc. IEEE Global Humanitarian Technol. Conf. (GHTC)*, Oct. 2015, pp. 219–225.
- [22] J. Dixon, L. Moran, J. Rodriguez, and R. Domke, "Reactive power compensation technologies: State-of-the-art review," *Proc. IEEE*, vol. 93, no. 12, pp. 2144–2164, Dec. 2005.
- [23] J. S. Daniels, "An integrated impedance biosensor array," Ph.D. dissertation, Dept. Elect. Eng. Stanford Univ., Stanford, CA, USA, 2010.
- [24] Y. Ishizuka-Katsura, T. Wazawa, T. Ban, K. Morigaki, and S. Aoyama, "Biotin-containing phospholipid vesicle layer formed on self-assembled monolayer of a saccharide-terminated alkyl disulfide for surface plasmon resonance biosensing," *J. Biosci. Bioeng.*, vol. 105, no. 5, pp. 527–535, May 2008.
- [25] A. G. Venkatesh, A. Sun, H. Brickner, D. Looney, D. A. Hall, and E. Aronoff-Spencer, "Yeast dual-affinity biobricks: Progress towards renewable whole-cell biosensors," *Biosens. Bioelectron.*, vol. 70, pp. 462–468, Aug. 2015.



Haowei Jiang (S'15) received the B.S. degree in electrical engineering from the Huazhong University of Science and Technology, Wuhan, China, in 2014. He is currently pursuing the Ph.D. degree in electrical engineering with the University of California at San Diego, La Jolla, CA, USA.

His research interests include low-power integrated RF/analog circuit design for sensing systems and biomedical devices.



Alexander Sun (S'14) received the B.S. degree in electrical engineering and computer science from the University of California at Berkeley, Berkeley, in 2012, and the M.S. degree in electrical and computer engineering from the University of California at San Diego, La Jolla, in 2014, where he is currently pursuing the Ph.D. degree.

His research focus is on electrochemical biosensors, electrochemical measurement techniques, and compact, low-power circuit design for biomedical, and point-of-care devices.



Alagarswamy G. Venkatesh received the B.Sc. degree in biochemistry from the University of Madras, India, the M.Sc. degree in biotechnology from Bharathidasan University, India, the M.Tech. degree in bioelectronics from Tezpur University, India, and the Ph.D. degree in physics from Bielefeld University, Germany.

During his doctoral research, he developed a novel platform to monitor DNA-Protein interactions in real-time. He was a Post-Doctoral Researcher with the University of Freiburg, Germany, where he developed low-cost smartphone-based devices for biomedical applications. At the University of California at San Diego, he developed smartphone-based electrochemical sensors for point-of-care application to detect HIV, Salmonella, and HCV infection. He is currently a Bio-Electronics Scientist with Roswell Biotechnologies Inc., San Diego, CA, USA, where he is involved in the development of nano-biosensors using CMOS integrated bio-molecular electronics platform.



Drew A. Hall (S'07–M'12) received the B.S. (Hons.) degree in computer engineering from the University of Nevada, Las Vegas, NV, USA, in 2005, and the M.S. and Ph.D. degrees in electrical engineering from Stanford University, Stanford, CA, USA, in 2008 and 2012, respectively.

From 2011 to 2013, he was a Research Scientist at the Integrated Biosensors Laboratory, Intel Corporation. Since 2013, he has been with Department of Electrical and Computer Engineering, University of California at San Diego, as an Assistant Professor.

His research interests include bioelectronics, biosensors, analog circuit design, medical electronics, and sensor interfaces.

Dr. Hall was a co-recipient of First Place in the Inaugural International IEEE Change the World Competition and First Place in the BME-IDEA Invention Competition, both in 2009. He received the Analog Devices Outstanding Designer Award in 2011, the Undergraduate Teaching Award in 2014, the Hellman Fellowship Award in 2014, and the NSF CAREER Award in 2015. He is also a Tau Beta Pi Fellow.